Advances in Modeling, Design, and Fabrication of Deep-Etched Multilayer Resonators

Raphael St-Gelais, Alexandre Poulin, and Yves-Alain Peter, *Senior Member, IEEE*

***Abstract*—We present recent advances in modeling, design, and fabrication of in-plane multilayer optical resonators fabricated by high aspect ratio etching of silicon. We first revisit the model of Gaussian beam divergence proposed by A. Lipson *et al.* to correct a mistake that leads to an underestimation of the losses affecting this type of resonator. Secondly, we discuss the influence of surface roughness at the silicon-air interfaces of multilayered structures. Roughness profiles—measured by white light interferometry on the sidewalls of silicon trenches etched by deep reactive ion etching (DRIE)—are presented. The single absorbing layer model of Carniglia *et al.* is used to predict the influence of the measured roughness (30 ± 5 nm RMS). This model is combined with the corrected model for Gaussian beam divergence and is compared with recent experimental results obtained for a new generation of deep-etched Fabry–Perot refractive index sensors. These sensors are fabricated using the contour lithography method, which is demonstrated to greatly improve the predictability of their optical characteristics. The combined model for roughness and divergence is found to correspond remarkably well with the experimental results, with predictions of loss and finesse of the resonances within an average error of 1.3 dB and 25%, respectively. We therefore expect the models and the simulations presented in this article to become a useful tool for the design of devices based on deep-etched multilayer resonators.**

***Index Terms*—Fabry-Perot resonators, integrated optics, optical resonators, scattering.**

I. Introduction

With the availability of high performance etching processes for silicon and with the need for cheap integrated optical components, silicon photonics is now attracting the attention of several research groups. In particular, multilayered silicon-air structures based on vertically etched high aspect ratio trenches are interesting since the in-plane configuration allows simple integration with electrostatic actuators, microfluidic systems, optical fibers and waveguides.

Because of the high refractive index contrast between silicon and air, mirrors based on these structures have a high reflectivity on a broad spectrum for very few Bragg periods. Two of such mirrors could therefore be used to form high finesse Fabry–Perot cavities. This possibility was investigated to fabricate tunable filters [2]–[5], refractive index sensors [6] and high quality factor resonators [7]. However, as reported in Table I, each of these devices suffers from high insertion loss and relatively low finesse ($\Im$). These performances make the tunable filters unusable for most of the targeted telecommunication applications. Such imperfections are less critical for refractive index sensors [6] than for tunable filters, but their detection limit could still be greatly improved by increasing the finesse of the resonance.

TABLE I
Reported Performances of Deep-Etched Fabry–Perot Resonators

Device type	Finesse	Peak transmission (dB)	Ref.
Tunable filter	39	-10	[4]
Tunable filter	24	-17	[5]
Refractive index sensor	7.1	-26	[6]
High quality factor cavity	20	-23	[7]

Therefore, it becomes necessary to identify clearly the influence of the different sources of losses in resonators based on deep-etched Bragg reflectors, with a particular emphasis on Fabry–Perot cavities coupled to optical fibers. In Section II, Gaussian beams are decomposed into plane waves to calculate the effect of beam divergence. The analysis is very similar to the one proposed in [1] but an important difference is outlined, which influences the results significantly. In Section III, measurements of surface roughness profiles on typical deep-etched sidewalls are presented. The single absorbing layer model [8] is proposed for the prediction of the losses due to the measured amount of roughness. In Section IV, the models for divergence and roughness are combined and are compared to experimental results obtained with a new generation of previously reported Fabry–Perot refractive index sensors [6]. These sensors are now fabricated by the contour lithography method [9]. We demonstrate that this technique improves the predictability of the dimensions of the optical resonators, and therefore of their optical characteristics. Finally, a brief discussion on other sources of loss that are not treated in the present text is presented in Section V.

II. Gaussian Beam Reflection and Transmission Through Ideal Deep-Etched Multilayers

A. Theory

A Fabry–Perot cavity based on two in-plane Bragg mirrors is presented in Fig. 1. Each of the Bragg mirrors is made of 2.5 silicon-air periods (P). If the thickness of each of the layers equals an odd multiple (m_{Si} for silicon and m_{Air} for air) of a quarter of a given wavelength (λ_c), the mirrors should have a broadband high reflectivity centered on λ_c. Fabry–Perot resonance will occur at that wavelength when a cavity of an integer multiple (m_{Gap}) of $\lambda_c/2$ is formed between the two mir-

Manuscript received November 18, 2011; revised March 08, 2012; accepted March 10, 2012. Date of publication March 15, 2012; date of current version April 09, 2012. This work was supported by the National Science and Engineering Research Council of Canada.

R. St-Gelais, A. Poulin, and Y.-A. Peter are with the Department of Engineering Physics, Ecole Polytechnique de Montréal, Montréal, Quebec H3C 3A7, Canada (e-mail: raphael.st-gelais@polymtl.ca; yves-alain.peter@polymtl.ca).

Color versions of one or more of the figures in this paper are available online at http://ieeexplore.ieee.org.

Digital Object Identifier 10.1109/JLT.2012.2191136

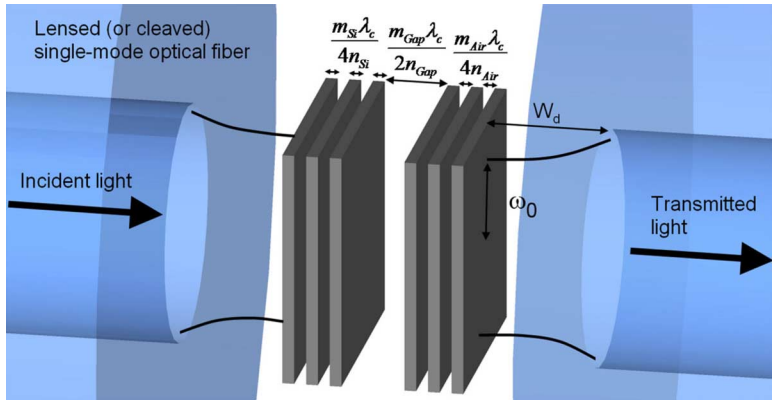

Fig. 1. Schematic representation of a $(m_{\mathrm{Si}}, m_{\mathrm{Air}}, m_{\mathrm{Gap}})$ Fabry–Perot cavity made of two mirrors of 2.5 silicon-air Bragg periods (P). The cavity is coupled at normal incidence to lensed or cleaved single-mode fibers of working distance W_d and Gaussian beam waist ω_0.

rors. In this text, as in [1], the dimensions of Fabry–Perot cavities will be written using a notation that includes the odd multiple of the silicon (m_{Si}) and air (m_{Air}) layers, and the integer multiple of the cavity (m_{Gap}) : $(m_{\mathrm{Si}}, m_{\mathrm{Air}}, m_{\mathrm{Gap}})$. The cavities are considered to be coupled at normal incidence to lensed or cleaved single-mode optical fibers, which working distance (W_d) and waist (ω_0) are presented in Fig. 1. For cleaved Corning® SMF-28™ fibers at near IR wavelength (1550 nm), the working distance and the waist are approximately zero and 5 μm, respectively.

Assuming that the beam incident on the multilayer structure of Fig. 1 is Gaussian and propagates along the z axis, its complex electric field distribution (neglecting the amplitude constant) can be expressed as in (1), where $q(z)$ is the complex beam parameter, k is the wavenumber, ω_0 is the beam waist and λ is the wavelength in the medium [10].

$$E(k,x,y,z) = \frac{q_0}{\omega_0}\frac{1}{q(z)}\exp\left(-ik\frac{x^2+y^2}{2q(z)} - ikz\right) \tag{1a}$$

with

$$q(z) = z + q_0 = z + i\frac{\pi\omega_0^2}{\lambda}. \tag{1b}$$

In order to compute the transmission through the multilayer system, the beam is decomposed into a two dimensional angular distribution of plane waves [11], [12] of transverse wavenumbers k_x and k_y. This is done by performing the Fourier transform presented in (2).

$$\begin{aligned}\tilde{E}(k,k_x,k_y,z) &= \iint E(k,x,y,z)e^{-i(k_x x+k_y y)}dxdy \\ &= -\frac{q_0}{\omega_0}\frac{2\pi i}{k}\exp\left(-i\frac{q(z)(k_x^2+k_y^2)}{k} - ikz\right)\end{aligned} \tag{2}$$

At this point, since the problem presents circular symmetry around the z axis, the two transverse components of the wavevector can be merged into a single variable using $k_t^2 = k_x^2 + k_y^2$ in (2).

For the transmission and the reflection of plane waves, the characteristic matrix formalism [13] is used. Each of the p layers of the assembly is modeled by a 2×2 matrix which is function of its thickness (d_r), its refractive index (N_r), of the angle of propagation in the layer (θ_r), and of the wavelength in vacuum (λ_0). The matrices are multiplied, starting with the output medium of admittance η_{out} and ending with the first layer of the assembly (at the interface with the incidence medium)

$$\begin{bmatrix} B \\ C \end{bmatrix} = \left\{\prod_{r=1}^{p}\begin{bmatrix} \cos\delta_r & (i\sin\delta_r)/\eta_r \\ i\eta_r\sin\delta_r & \cos\delta_r \end{bmatrix}\right\}\begin{bmatrix} 1 \\ \eta_{\mathrm{out}} \end{bmatrix} \tag{3a}$$

with

$$\delta_r = 2\pi N_r d_r\cos\theta_r/\lambda_0 \tag{3b}$$

$$\eta_r = N_r\cos\theta_r(\text{for } s \text{ polarization}) \tag{3c}$$

$$\eta_r = N_r/\cos\theta_r(\text{for } p \text{ polarization}). \tag{3d}$$

In (3), the cosines of the angle of propagation (θ_r) in each layer can be expressed in term of the refractive index of the layer, of the wavelength in vacuum (λ_0) and of the transverse component of the wavevector (k_t) which is independent of the refractive index of the medium. This is presented in (4), which is simply an alternative notation of Snell's law of refraction.

$$\cos\theta_r = \sqrt{1-(k_t\lambda_0/2\pi N_r)^2} \tag{4}$$

Using (4) in (3), the amplitude reflection (r) and transmission (t) coefficients can be obtained [13] as a function of k_t, λ_0 and of the admittance of the incident medium (η_{inc})

$$\begin{aligned} r(\lambda_0,k_t) &= \frac{\eta_{\mathrm{inc}}B - C}{\eta_{\mathrm{inc}}B + C}, \\ t(\lambda_0,k_t) &= \frac{2\eta_{\mathrm{inc}}}{\eta_{\mathrm{inc}}B + C}. \end{aligned} \tag{5}$$

Finally, using the plane wave distribution of (2) combined with the plane wave reflection and transmission coefficients of (5), it is possible to obtain the reflectivity and the transmission of the complete system.

From this point, it is assumed that the distance between the optical fibers and the multilayer system is equal to the lensed

fibers working distance (W_d), as depicted in Fig. 1. In the current notation, this involves taking $z = 0$ in (2). The important example of a cleaved single-mode optical fiber should be represented accurately by this assumption if the fibers are placed as close as possible to the multilayer assembly ($W_d \approx 0$). It is also assumed that, at the first and last interfaces of the multilayer system, the medium is air and has unit refractive index (i.e., $\eta_{\rm inc} = \eta_{\rm out} = \eta_{\rm vacuum}$).

The fiber-to-fiber transmission and reflection spectra (T, R) are obtained by multiplying the incident electric field distribution of (2) by the coefficients of (5), and by calculating the overlap integral with the output optical fiber

$$T(\lambda_0), R(\lambda_0) = \frac{|\langle \tilde{E}_{\rm out} | \tilde{E}_{\rm fiber} \rangle|^2}{\langle \tilde{E}_{\rm fiber} | \tilde{E}_{\rm fiber} \rangle}^2 \tag{6a}$$

with

$$\tilde{E}_{\rm fiber} = \tilde{E}\left(\frac{2\pi}{\lambda_0}, k_t, 0\right) \tag{6b}$$

$$\tilde{E}_{\rm out}\left(\frac{2\pi}{\lambda_0}, k_t, 0\right) = \tilde{E}_{\rm fiber} \cdot t(\lambda_0, k_t)\ (\text{transmission}) \tag{6c}$$

$$\tilde{E}_{\rm out}\left(\frac{2\pi}{\lambda_0}, k_t, 0\right) = \tilde{E}_{\rm fiber} \cdot r(\lambda_0, k_t)\ (\text{reflection}). \tag{6d}$$

At this point, a choice must be made whether to use the plane wave coefficients (t, r) calculated for s or p polarization using (3a)–(5). The Gaussian beam expression of (1) is a linear approximation, which imply that the components of the polarization that are parallel to the main direction of propagation (the z axis) are considered to be weak and are neglected [14]. Therefore, if the Gaussian beam approximation is appropriate to treat the current problem, the use of whether the s or the p coefficients of transmission and reflection should not influence the calculated results (for the case of a beam at normal incidence). This is effectively the case. For all the following calculations, using s or p coefficients yields almost exactly the same spectra. In the worst case (minimum beam waist and highest number of periods for each Bragg mirrors) the difference at peak transmission is less than 0.3 dB.

The bracket notation in (6a) denotes the scalar product of two electric fields. From the properties of Fourier transforms, it can be calculated directly in the k_t space without going back to the (x, y) space (see Parseval's theorem [15]). From the circular symmetry of the problem, this integration can be performed in polar coordinate.

$$\langle \tilde{E}_1 | \tilde{E}_2 \rangle = 2\pi \int_0^k \tilde{E}_1 \tilde{E}_2^* k_t dk_t \tag{7}$$

The analysis of (1)–(6) is equivalent to the one published by A. Lipson *et al.* [1]. These authors must of course be credited for the original idea, at least in the context of deep-etched multilayer resonators (similar developments can be found to treat the deformation of beams incident on multilayer structures [11]). However, in [1, eq. (2)], it appears that the integration was performed only along k_t without considering the circular symmetry of the problem. In the current notation, this is equivalent to replace $k_t \mathrm{d}k_t$ in (7) by $\mathrm{d}k_t$.

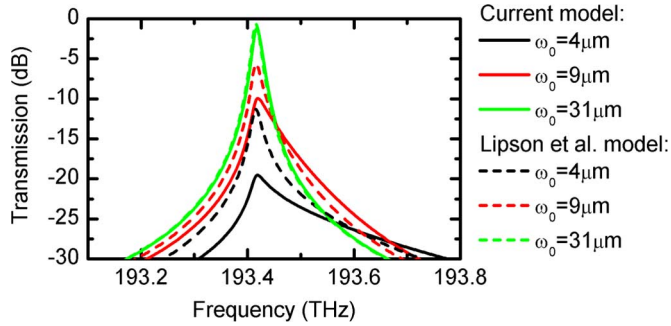

Fig. 2. Transmission spectra of a $(m_{\rm Si}, m_{\rm Air}, m_{\rm Gap}) = (21, 5, 2)$ Fabry–Perot filter of 2.5 periods mirrors for various Gaussian beam waists. Plain lines: calculation using the current proposed model. Dashed lines: calculations removing the k_t factor in (7), as is supposed to be an error in Lipson *et al.* [1] original model. For large beam waists ($\omega_0 = 31$ μm) the effect of divergence is negligible and the curves obtained with the two models are superimposed.

This error can have important consequences on the calculated response of resonators based on deep-etched Bragg reflectors. In Fig. 2, the transmission of a Fabry–Perot cavity based on 2.5 periods mirrors is calculated for different beam waist using the formulation of the overlap integral of (7), and also by removing the k_t factor, as appears to be the case in [1]. The axis limits are set to reproduce as exactly as possible the Fig. 2 of [1]. For a 31 μm beam waist, the effect of divergence is negligible and both models yield the same transmission spectrum. However, for a 4 μm waist, the difference between the peak transmissions is nearly 10 dB.

In order to validate which of the current or of Lipson *et al.* [1] model is accurate, a simple numerical experiment was also performed. The developed algorithm (1)–(7) was used to calculate the coupling loss between two optical fibers separated by an air layer. This is done using a single air layer of any given thickness in (3). With the current model, the results match perfectly the equations developed in [16]. Removing the k_t factor in (7) yields the square root of the value of [16]. This can be understood by noting that removing k_t in (7) is equivalent to considering divergence in only one (say x) of the two transverse dimensions (x, y).

B. Discussion

The difference between the two models, outlined in Fig. 2, justifies the formulation of new design rules for resonators based on deep-etched Bragg reflectors, especially since it affects particularly the important case of cleaved single-mode optical fibers ($\omega_0 \approx 5$ μm at $\lambda_0 = 1550$ nm).

These are presented in Fig. 3, where the peak transmission and the finesse $(\Im)$ are reported as a function of Gaussian beam waist, for a variety of Fabry–Perot resonators having resonance peaks centered on $\lambda_c = 1550$ nm. The finesse is defined as the ratio of the free spectral range (FSR) and of the full width at half maximum (FWHM) of the resonance peaks ($\Im = \mathrm{FSR}/\mathrm{FWHM}$). The FWHM is determined by inspection of the simulated resonance. For long cavities (large $m_{\rm Gap}$) the thickness of the mirrors is negligible compared to the

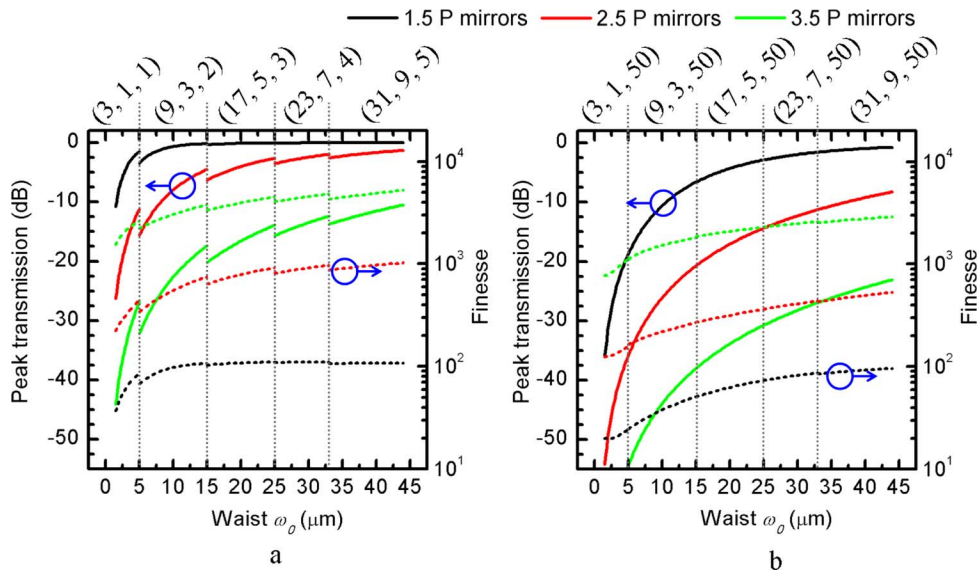

Fig. 3. Peak transmission (plain lines) and finesse (dashed lines) of a Fabry–Perot resonance occurring at the center of a reflection bandwidth, set at $\lambda_c = 1550$ nm, as a function of the Gaussian beam waist, and for various silicon-air periods (P) in each mirror. The $(m_{\mathrm{Si}}, m_{\mathrm{Air}}, m_{\mathrm{Gap}})$ dimension parameters are adjusted to maintain a 1:30 maximal aspect ratio criterion for the etched trenches. (a) Simulations performed for shorter cavity lengths (e.g.: tunable filters). (b) Simulations performed for longer cavities (e.g.: sensors).

cavity length and the FSR can be determined solely from the m_{Gap} value using the simplification in (8). For shorter cavities (small m_{Gap}), however, the phase shift upon reflection on the mirrors becomes significant and the FSR must be calculated by inspection of the transfer matrix simulations using

$$FSR = \frac{\Delta\lambda_c}{\Delta m_{\mathrm{Gap}}} = \frac{\lambda_c}{2}\frac{\Delta\lambda_c}{\Delta(n_{\mathrm{Gap}}l)} \overset{\text{large } m_{\mathrm{Gap}}}{\longrightarrow} \frac{\lambda_c^2}{2n_{\mathrm{Gap}}l} = \frac{\lambda_c}{m_{\mathrm{Gap}}} \quad (8)$$

where $l = m_{\mathrm{Gap}}\lambda_c/2n_{\mathrm{Gap}}$ is the distance between the mirrors.

In Fig. 3, the dimension constants $(m_{\mathrm{Si}}, m_{\mathrm{Air}}, m_{\mathrm{Gap}})$ of the resonators are increased progressively with the beam waist to take into account the limitations of deep etching techniques. When the beam diameter $(2\omega_0)$ becomes more than 25 times greater than the thickness of the air layers $(m_{\mathrm{Air}}\lambda_c/4)$, the dimension constant m_{Air} is increased to the next odd integer (i.e., the required aspect ratio is kept below 1:30). The thickness of the silicon layers (related to the integer m_{Si}) is also adjusted to respect the same aspect ratio criterion.

In Fig. 3(a), simulations are performed for short cavity lengths (low m_{Gap}), which are more representative of works related to tunable Fabry–Perot filters [2]–[5]. Increasing the number of silicon-air periods increases the reflectivity of the Bragg mirrors and therefore increases the finesse. However, this also confines the light more strongly within the cavity and the losses due to divergence increase. For 1.5 period mirrors, it is theoretically possible to reach losses lower than -3 dB for the typical beam waist of a cleaved single-mode fiber ($\sim$5 μm). For 2.5 period mirrors, the same level of losses is obtained only with beam waists of 23 μm or higher. For 3.5 period mirrors, the same level of loss could not be obtained unless using inconvenient etch depths (>100 μm). Maintaining good surface quality and constant layer thickness on such a high depth would be extremely challenging. Moreover, as the $(m_{\mathrm{Si}}, m_{\mathrm{Air}})$ dimension constants increase, the width of the reflection band (i.e., the range around λ_c on which high finesse Fabry–Perot resonance occurs) reduces significantly. For example, at dimensions higher than $(m_{\mathrm{Si}}, m_{\mathrm{Air}}) = (23, 7)$, the reflection bandwidth becomes lower than 80 nm and it becomes impossible to cover more than one of the 40 nm wide S, C and L telecommunication bands.

In Fig. 3(b), simulations are performed for longer cavity lengths (large m_{Gap}), which are more representative of the work related to Fabry–Perot refractive index sensors [6]. The losses are more important in this case since light diverge on a longer distance during each round trip in the cavity. Losses are however less critical for sensors than for tunable filters. Their design, for the highest possible finesse, should therefore also be dictated by the highest amount of loss that is acceptable with a given measurement setup, by the operation bandwidth, and by other considerations such as the amount of surface roughness, as presented in the next section.

III. Surface Roughness in Deep-Etched Trenches

Various well documented fabrication methods can be used to minimize the amount of surface roughness in deep-etched trenches. Most of the etching processes are performed in inductively coupled plasma reactors (ICP). At room temperatures, fluorine based ICP chemistry can be optimized to reduce the characteristic scalloping effect induced by chopping between passivation and etching gases [17]–[20]. Both gases can also be used in room temperature mixed processes [21], [22], avoiding completely the scalloping effect at the expense of poorer selectivity to the etch mask. At cryogenic temperatures, however, mixed process can yield high selectivity and smooth sidewalls can be obtained in high aspect ratio structures [17], [21], [23], [24]. Other techniques, not based on ICP reactors, also allow etching of smooth high aspect ratio trenches such as electrochemical etching in hydrofluoric acid (HF) [25] and preferential etching

of (110) silicon wafers along crystallographic planes [26], [27]. Finally, post-processing techniques such as thermal oxidation [28] and crystallographic planes selective etching [4], [29]–[31] can be used to reduce surface roughness in deep-etched silicon trenches.

A. Surface Roughness Model

Despite this variety of methods, few analyses were carried out to quantify the optical properties of deep-etched multilayered structures as a function of the amount of surface roughness at the material interfaces. In [29], the analysis is limited to a single silicon slab and does not consider light divergence. In [32], surface roughness is treated as a random variation of the layers thickness (i.e., scattering by surface roughness is neglected). This kind of analysis is usually appropriate for most Fabry–Perot cavities [33]. However, for silicon-air Bragg reflectors, the refractive index contrast between each layer is much higher than for any multilayer mirror fabricated by thin film deposition. As this contrast increases, the amount of light that is scattered by surface roughness is expected to become significant. Additionally, computing a random distribution of layer thicknesses together with the model of Gaussian beam divergence (Section II) would be tedious. For each component of the plane wave decomposition, the transfer matrices would have to be calculated several times to consider the random distribution, which would imply inconvenient computation delays.

For these reasons, the use of the model of Carniglia *et al.* [8] is proposed. A single absorbing layer is added at each material interface as a function of its surface roughness RMS (root mean square) value (σ). The thickness (d_R) of the layer is function of σ as $d_R = 2\sigma$. The real part (n_R) of the refractive index of the layer (n) is given by Drude effective medium approximation [8]. An imaginary part (k_R) is added to n in order to take into account the reduced transmission and reflection predicted by the scalar scattering theory. The expression of n, for silicon and air as the adjacent mediums is given by

$$n = n_R - ik_R = \sqrt{\frac{n_{\mathrm{Air}}^2 + n_{\mathrm{Si}}^2}{2}} - i\frac{\pi}{2\sqrt{2}}\frac{(n_{\mathrm{Air}} - n_{\mathrm{Si}})^2(n_{\mathrm{Air}} + n_{\mathrm{Si}})}{\sqrt{n_{\mathrm{Air}}^2 + n_{\mathrm{Si}}^2}}\frac{d_R}{\lambda_0}. \tag{9}$$

B. Roughness Measurement

The single absorbing layer model requires the knowledge of the amount of surface roughness at the silicon-air interfaces, which is measured using a white light interferometric surface profiler (Fogale Photomap 3-D optical profiler). Cleaved silicon-air multilayer test structures (Fig. 4(a)), fabricated simultaneously with the refractometer of Fig. 8 and having the same silicon-air layers dimensions, are used for the measurements. The measured profile is presented in Fig. 4(b). The amount of surface roughness is evaluated on a 20×20 μm surface, which is centered on the expected position of the core of the single mode optical fiber that will be used for the characterization of the Fabry–Perot cavities. The measurement yields a value of 30 ± 5 nm RMS. The 5 nm uncertainty was determined statistically by varying the size and the position of the measurement area, and by repeating the measurement on other test structures.

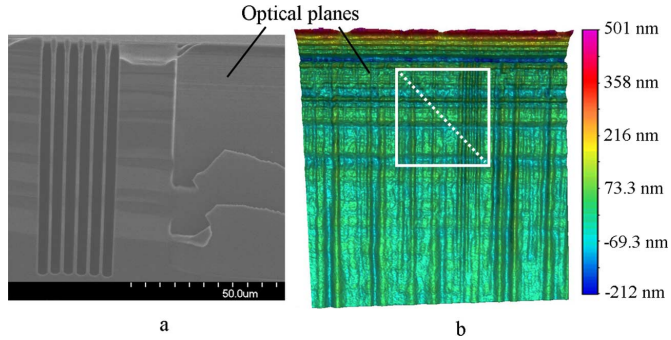

Fig. 4. (a) Scanning electron micrograph cross section and front view of cleaved multilayer test structures etched using the same DRIE process as for the Fabry–Perot cavity of Fig. 8. (b) Measured roughness profile of an etched optical plane. The roughness is evaluated within a 20×20 μm area (white square) centered on the expected position of the core of the single mode optical fiber that will used for the optical characterization.

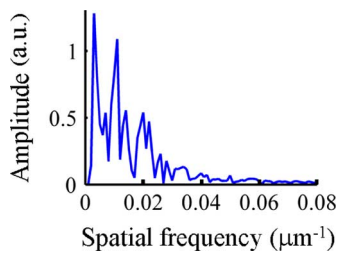

Fig. 5. One dimensional Fourier transform of the measured profile (along the white dashed line of Fig. 4(b) showing that the measured roughness is dominated by large scale harmonics.

The one dimensional Fourier transform of the measured profile is also calculated, following the diagonal of the area of interest (i.e., the white dashed line in Fig. 4(b)). Its amplitude, presented in Fig. 5, indicates that the measured RMS roughness is mainly dominated by large-scale harmonics (i.e., low spatial frequency roughness). This is an important parameter since it can be demonstrated [34] that the model of [8] is valid for large scale roughness harmonics (T_m), respecting the criterion $1/T_m < 1/\lambda_0 n_2$, where n_2 is the higher refractive index of the assembly (i.e., n_{Si} in the present case). The roughness measurement method should therefore be chosen carefully in order to ensure that the measured overall RMS roughness contains mainly large scale roughness harmonics, which cause scattering and are taken into account by the model. For example, as described in [35], atomic force microscopy measurements tend to contain mainly small scale harmonics that are not take into account by the current model.

IV. Experimental Validation

A. Fabrication of Deep-Etched Fabry–Perot Resonators by Contour Lithography

In order to compare the developed models for roughness and divergence with experimental results, a new generation of Fabry–Perot refractive index sensors previously described in [6] was fabricated. Instead of using single lithography and DRIE steps, the two masks contour lithography method

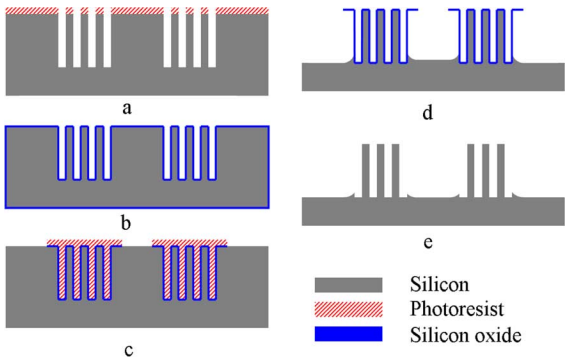

Fig. 6. Schematic representation of the fabrication process used for the Fabry–Perot refractometer of Fig. 8. (a) 1st lithography & DRIE, (b) Dry oxidation, (c) 2nd lithography & Buffered HF etching, (d) Isotropic SF_6 plasma etching & O_2 Resist stripping, (e) Buffered HF etching.

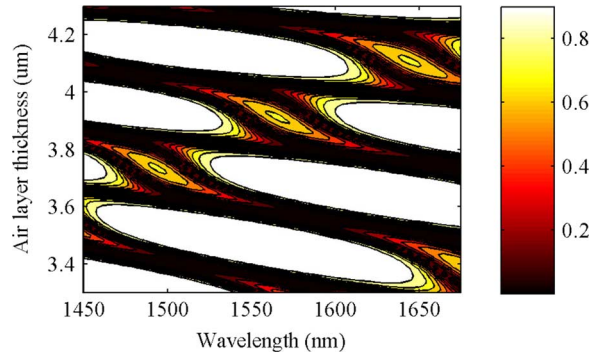

Fig. 7. Calculated reflectivity of a 2.5 periods mirror having a constant silicon-air period of 4.7 μm, as a function of wavelength and of the air layers thickness. High reflectivity (>0.9) covering the desired wavelength range (1500 to 1600 nm) occurs for air layers thicknesses around 3.5 or 4.15 μm.

TABLE II
DRIE PARAMETERS

Parameter	Etching Step	Passivation step
Time (s)	6	4
ICP power (W)	450	450
Forward power (W)	18	10
SF_6 flow (sccm)	65	0
C_4F_8 flow (sccm)	4	65
O_2 flow (sccm)	6	0
Chuck temperature (^oC)	0	0
Chamber pressure (mTorr)	15	15

proposed in [9] was used to fabricate separately the optical parts (multilayer mirrors) and the larger features (optical fiber alignment grooves, microfluidics). The fabrication steps are summarized here but [9] should be consulted for further details, if needed.

A schematic representation of the fabrication process is presented in Fig. 6. The mirrors and the contour of the larger openings (optical fiber grooves, microfluids) are first etched to a depth of 80 μm by deep reactive ion etching (step a) in an ICP180-100 plasma reactor (Oxford Instruments inc.). The chamber parameters for the etching and passivation steps (applied 415 times each) are given in Table II. After a dry oxidation step ($\sim$150 nm SiO_2) to protect the optical parts (step b), a second mask is used to define the larger openings (step c). The oxide is etched in buffered hydrofluoric acid (HF) and the larger features are etched by isotropic SF_6 plasma etching in the ICP plasma reactor (step d). The remaining oxide is finally etched in buffered HF (step e).

The contour lithography method was originally proposed as a technique to integrate nanoscale trenches with wider openings that require significantly different plasma etching conditions. We would like to outline another advantage of the technique, which was not reported in [9], and which motivated its use in the present case. When the mirrors are etched separately from the larger features, all the openings of the first photomask (used for step a in Fig. 6) have the same width. This width will change upon fabrication because of diffraction during photolithography and undercut during plasma etching. However, since they all have the same initial width, all the air layers that form a set of mirrors can be assumed to have the same final thickness. Conversely, all the silicon layers in Fig. 6 can also be assumed to have identical thicknesses. Moreover, the thickness of a silicon-air period in Fig. 6 becomes a constant that is not affected by diffraction and undercutting. There is therefore only one unknown (i.e., the air layers thickness) to consider during the design of the photomask and much more predictable optical characteristics can be obtained.

For the results presented in the next section, the silicon-air period of each device on the photomask was fixed to a constant value of 4.7 μm. Several different air layer thicknesses were designed to ensure that some devices yield a high mirror reflectivity in the wavelength range (1500 nm to 1600 nm) used for characterization and refractive index sensing. Indeed, as presented in Fig. 7 for silicon-air periods of 4.7 μm, high mirror reflectivity is expected in the targeted range for air layers thicknesses around 3.5 μm or 4.15 μm.

B. Results and Discussion

A Fabry–Perot refractometer fabricated by contour lithography and based on 2.5 periods mirrors is presented in Fig. 8(a). Similar devices, based on 1.5 periods mirrors, were also fabricated and characterized. The measured and calculated transmission spectra, for both designs, are presented in Fig. 8(b). As targeted, the reflection band of the mirrors span across the 1500–1600 nm wavelength range, where the sharpest resonance peaks are visible. The results were obtained for nominal (i.e., dimensions on the photomask) thicknesses of the air and silicon layers of 2.8 μm and 1.9 μm, respectively, and for a nominal gap between the mirrors of 35 μm.

The nominal dimensions are of course different from those of the fabricated devices. The dimensions used to simulate the devices in Fig. 8(b) were determined using the calculations of Fig. 7. The silicon-air period was kept constant (4.7 μm) and the air layer thickness was adjusted to reach the best match between the position of the simulated and measured reflection bands. For the 2.5 P devices, the best match was obtained with air layer thicknesses of 4.105 (i.e., 0.595 μm silicon layers). The gap between the mirrors, which was designed at 35 μm, was consequently increased to 36.305 μm. The characterized 1.5 P device apparently experienced a little more diffraction during lithography and/or undercut during DRIE since the best fit was obtained for dimensions of 4.115 μm (air), 0.585 μm (silicon) and

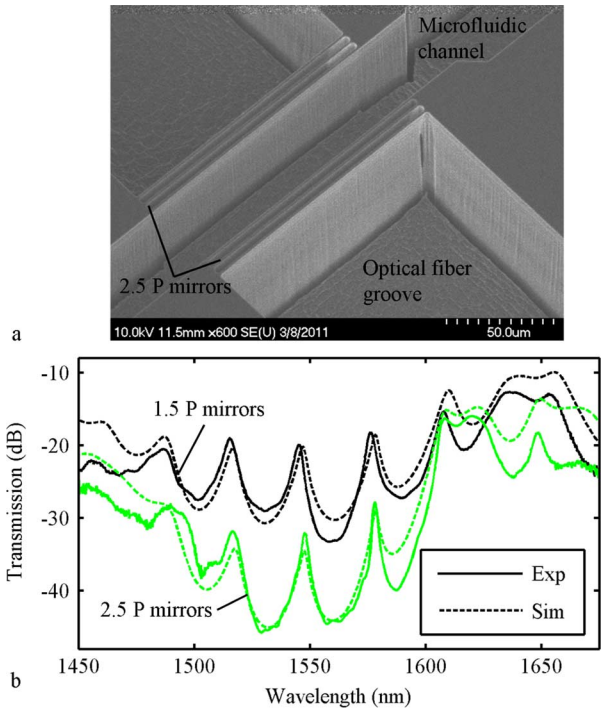

Fig. 8. (a) Scanning electron micrograph of a Fabry–Perot refractometer fabricated by contour lithography and based on 2.5 periods (P) mirrors. (b) Experimental and simulated transmission spectra of Fabry–Perot refractometers based on 2.5 P (green) and 1.5 P mirrors (black).

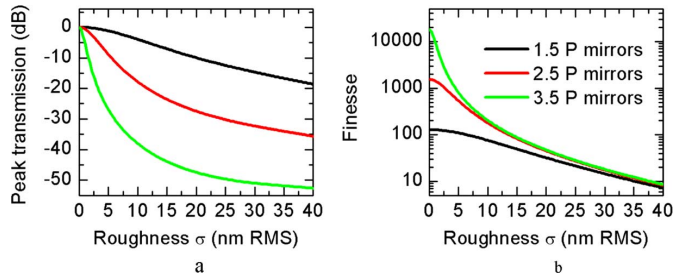

Fig. 9. Peak transmission (a) and finesse (b) of a $(m_{\mathrm{Si}}, m_{\mathrm{Air}}) = (17, 5)$ Fabry–Perot resonator of infinite beam waist (ω_0) as a function of surface roughness and for different numbers of Bragg periods (P) in each mirror.

36.315 μm (gap). This difference could be due to slightly inhomogeneous plasma and/or photomask-wafer contact during photolithography.

To include the effect of surface roughness, a thickness of $2\sigma = 2 \times 30$ nm RMS is subtracted from each layer and a 2σ thick absorbing layer, described by (9), is added at each silicon-air interface. The devices are characterized using cleaved Corning® SMF-28™ single mode optical fibers. The effect of divergence is therefore taken into account by performing the simulations with a 5 μm Gaussian beam waist.

As shown in Fig. 8(b), the simulations correspond closely to the measured transmission spectra. The maximum transmission of the main resonance peaks (i.e., the peaks located between 1500 nm and 1600 nm) is estimated correctly, within an average error of 1.3 dB. The finesses $(\Im)$ of the resonance peaks also correspond to the measurements, within an average error of 25%. The difference between the simulated and experimental results may be due to the glass-air interfaces of the cleaved optical fibers, for which the exact positions are unknown, to the uncertainty on the dimensions of the layers on the photomask (<50 nm according to the mask supplier, Benchmark Technologies), to the uncertainty on the amount of surface roughness (5 nm RMS), or to other imperfections that are not taken into account in the model (see next section).

The model was also used to interpret other structures that are not presented to lighten the text. It allowed the prediction of the finesse within less than 30% of uncertainty and of the losses within 3 dB of uncertainty for the main peaks of the Fabry–Perot tunable filter presented in [5]. It also allowed the interpretation of the loss of the Gires–Tournois interferometer presented in [36] within less than 3 dB of uncertainty. Finally, one-dimensional photonic crystals fabricated by other groups [26], [32] were also simulated. The model allowed the prediction of a decrease of the reflectivity in the bandgap region due to light scattering, an effect that could not be predicted in [32] by treating roughness as a random variation of the layer thicknesses.

In Fig. 8, the highest finesse $(\Im = 12.1)$ is obtained at $\lambda = 1578$ nm for the cavity based on 2.5 periods mirrors. This is a 70% increase (see Table I) compared to previous works on refractive index sensors [6] having similar dimensions. It is possible that the contour lithography fabrication method allowed lower surface roughness on the silicon surfaces that face large openings (optical fiber alignment grooves, microfluidic channels), as previously reported [9]. It is also possible that the oxidation step of the contour lithography method (Fig. 6, step b) reduced surface roughness at the silicon-air interfaces [28]. The reached finesse is, however, lower than what was previously obtained with Fabry–Perot cavities based on smaller gaps [4], [5] or incorporating focusing optics [7]. The impact of divergence was most likely less important in these cases, which allowed higher finesses, as predicted in Fig. 3 for shorter cavities (lower m_{Gap}).

In Fig. 8(b), the finesse reached with 2.5 P mirrors $(\Im = 12.1)$, is 70% higher than with the 1.5 P device $(\Im = 7.0)$. However, this relatively modest increase occurs at the expense of signal losses of more than 10 dB. This result tends to indicate that, for a given amount of surface roughness, there is an optimal number of layers above which small finesse improvements occur at the expense of important signal losses. This condition can be predicted using the roughness model. In Fig. 9, the finesse and peak transmission at resonance are reported as a function of surface roughness for resonators based on various numbers of silicon-air periods. The calculations are performed with $(m_{\mathrm{Si}}, m_{\mathrm{Air}}) = (17, 5)$ nominal mirrors dimensions, but the results would be essentially the same for any other $(m_{\mathrm{Si}}, m_{\mathrm{Air}})$ odd integers. The calculations are also valid for any cavity length (i.e., any m_{Gap} dimension constant). Above a given amount of roughness, the reflectivity of the Bragg mirrors, and hence the finesse, is not increased anymore by adding additional Bragg periods. For example, in Fig. 9, the finesse for 2.5 and 3.5 period mirrors is essentially the same when surface roughness is superior to 10 nm RMS. Therefore, when Bragg mirrors are to be used in transmission (such as for Fabry–Perot filters) the choice of the number of Bragg periods should be dictated by the lowest level of surface roughness that can be reached experimentally.

V. Other Sources of Loss

The correspondence between the model and the experimental results in Fig. 8 tends to demonstrate that, for the reported devices, surface roughness and beam divergence are the dominant sources of loss. However, if surface roughness was decreased and if a larger beam waist was used, other sources of loss would probably become non-negligible.

For Fabry–Perot cavities based on stacked thin films reflectors, curvature and imperfect parallelism between the mirrors affect the finesse in a similar way as surface roughness does. For example, a 10 nm deviation of the distance between the mirrors due to imperfect parallelism—which would corresponds to an angle of 0.06° for a mirror diameter of 10 μm—is expected to induce roughly the same decrease of finesse as the presence of 10 nm RMS surface roughness [33].

In the particular case of resonators based on deep-etched Bragg reflectors, curvature or imperfect parallelism between the silicon-air interfaces should also affect the finesse. In [1], imperfect parallelism is considered to occur between the two mirrors (i.e., verticality deviations inside the Bragg mirrors are neglected) and is simulated by summing the amplitude and phase of the Gaussian beam after each round-trip in the cavity. For cavities based on 2.5 periods Bragg mirrors, a deviation of verticality of 0.005° is expected to induce roughly the same decrease of finesse as the presence of 5 to 10 nm of surface roughness in Fig. 9. However, for deep-etched Fabry–Perot resonators, the influence of imperfect parallelism between the Bragg mirror material interfaces, rather than between the mirrors themselves [1], [33] is not treated in the literature and is therefore a subject that remains to be explored.

VI. Conclusion

Gaussian beam divergence in deep-etched multilayer resonators was demonstrated to induce more loss than what was previously reported in [1]. The underestimation is especially important for smaller beam waist, reaching around 10 dB for the waist of cleaved single mode optical fibers. The model for divergence was corrected and was combined with the single layer model for surface roughness proposed in [8].

The combined model was compared with the measured transmission spectra of Fabry–Perot resonators fabricated using the contour lithography method [9]. This technique—which was originally intended for the integration of nanometer and millimeter-scale structures—is also found to greatly improve the predictability of the dimensions of deep-etched multilayered structures. This improvement allowed the comparison of simulated and experimental results without errors due to undetermined optical layers thicknesses.

The correspondence of the combined model with experimental results tends to demonstrate that surface roughness is among the dominant source of loss in deep-etched silicon-air multilayer resonators, at least for the reported devices. We therefore conclude that the presence of surface roughness, which is inherent to most silicon etching techniques, should be taken into account during the design of deep-etched multilayer resonators. The single absorbing layer model [8]—coupled with roughness profiles measured by white light interferometric surface profiling—is found to be appropriate for this purpose. We demonstrated that it can conveniently be combined with the corrected model for Gaussian beam divergence. It also takes into account light scattering, which is expected to be important for the large refractive index contrast between silicon and air.

In summary, the combined model for beam divergence and surface roughness presented in this article is found to correspond closely to experimental results. It is therefore expected to provide useful design guidelines for the optimization of devices based on deep-etched optical resonators. We also provide a design technique—based on the contour lithography fabrication method—that allows the fabrication of deep-etched multilayer structures having predictable dimensions and optical characteristics. This design technique could therefore lead to an improvement of the fabrication yield of deep-etched optical resonators.

References

[1] A. Lipson and E. M. Yeatman, "Low-loss one-dimensional photonic bandgap filter in (110) silicon," *Opt. Lett.*, vol. 31, pp. 395–397, 2006.

[2] S. S. Yun and J. H. Lee, "A micromachined in-plane tunable optical filter using the thermo-optic effect of crystalline silicon," *J. Micromech. Microeng.*, vol. 13, pp. 721–725, 2003.

[3] B. Saadany, M. Malak, M. Kubota, F. Marty, Y. Mita, D. Khalil, and T. Bourouina, "Free-space tunable and drop optical filters using vertical Bragg mirrors on silicon," *IEEE J. Sel. Top. Quantum Electron.*, vol. 12, pp. 1480–1487, 2006.

[4] A. Lipson and E. M. Yeatman, "A 1-D photonic bandgap tunable optical filter in (110) silicon," *J. Microelectromech. Syst.*, vol. 16, pp. 521–527, 2007.

[5] J. Masson, R. St-Gelais, A. Poulin, and Y.-A. Peter, "Tunable fiber laser using a MEMS-based in plane Fabry-Pérot filter," *IEEE J. Quantum Electron.*, vol. 46, pp. 1313–1319, 2010.

[6] R. St-Gelais, J. Masson, and Y.-A. Peter, "All-silicon integrated Fabry–Perot cavity for volume refractive index measurement in microfluidic systems," *Appl. Phys. Lett.*, vol. 94, p. 243905, 2009.

[7] M. Malak, F. Marty, N. Pavy, Y.-A. Peter, A.-Q. Liu, and T. Bourouina, "Cylindrical surfaces enable wavelength-selective extinction and sub-0.2 nm linewidth in 250 μm-Gap Silicon Fabry-Pérot cavities," *J. Microelectromech. Syst.*, vol. 21, pp. 171–180, 2012.

[8] C. K. Carniglia and D. G. Jensen, "Single-layer model for surface roughness," *Appl. Opt.*, vol. 41, pp. 3167–3171, 2002.

[9] Y. Mita, M. Kubota, T. Harada, F. Marty, B. Saadany, T. Bourouina, and T. Shibata, "Contour lithography methods for DRIE fabrication of nanometre-millimetre-scale coexisting microsystems," *J. Micromech. Microeng.*, vol. 16, pp. S135–S141, 2006.

[10] A. E. Siegman, *Lasers*. Sausalito, CA: University Science Books, 1986.

[11] G. D. Landry and T. A. Maldonado, "Gaussian beam transmission and reflection from a general anisotropic multilayer structure," *Appl. Opt.*, vol. 35, pp. 5870–5879, 1996.

[12] J. W. Goodman, *Introduction to Fourier Optics*. New York: Roberts & Company Publishers, 2005.

[13] H. A. Macleod, *Thin-Film Optical Filters*. New York: Institute of Physics Publishing, 2001.

[14] E.-G. Neumann, *Single-Mode Fibers*. New York: Springer-Verlag, 1988.

[15] G. B. Arfken and H. J. Weber, *Mathematical Methods for Physicists*, 5th ed. San Diego, CA: Harcourt Academic Press, 2001.

[16] S. Yuan and N. A. Riza, "General formula for coupling-loss characterization of single-mode fiber collimators by use of gradient-index rod lenses," *Appl. Opt.*, vol. 38, pp. 3214–3222, 1999.

[17] F. Marty, L. Rousseau, B. Saadany, B. Mercier, O. Francais, Y. Mita, and T. Bourouina, "Advanced etching of silicon based on deep reactive ion etching for silicon high aspect ratio microstructures and three-dimensional micro- and nanostructures," *Microelectron. J.*, vol. 36, pp. 673–677, 2005.

[18] B. Volland, F. Shi, P. Hudek, H. Heerlein, and I. W. Rangelow, "Dry etching with gas chopping without rippled sidewalls," *J. Vac. Sci. Technol., B*, vol. 17, p. 2768, 1999.

[19] M. Chabloz, Y. Sakai, T. Matsuura, and K. Tsutsumi, "Improvement of sidewall roughness in deep silicon etching," *Microsyst. Technol.*, vol. 6, pp. 86–89, 2000.

[20] H. C. Liu, Y. H. Lin, and W. Hsu, "Sidewall roughness control in advanced silicon etch process," *Microsyst. Technol.*, vol. 10, pp. 29–34, 2003.
[21] C. C. Welch, A. L. Goodyear, T. Wahlbrink, M. C. Lemme, and T. Mollenhauer, "Silicon etch process options for micro- and nanotechnology using inductively coupled plasmas," *Microelectron. Eng.*, vol. 83, pp. 1170–1173, 2006.
[22] K. Solehmainen, T. Aalto, J. Dekker, M. Kapulainen, M. Harjanne, and P. Heimala, "Development of multi-step processing in silicon on insulator for optical waveguide applications," *J. Opt. A: Pure Appl. Opt.*, vol. 8, pp. S455–S460, 2006.
[23] M. J. de Boer, J. G. E. Gardeniers, H. V. Jansen, E. Smulders, M. J. Gilde, G. Roelofs, J. N. Sasserath, and M. Elwenspoek, "Guidelines for etching silicon MEMS structures using fluorine high-density plasmas at cryogenic temperatures," *J. Microelectromech. Syst.*, vol. 11, pp. 385–401, 2002.
[24] M. W. Pruessner, W. S. Rabinovich, T. H. Stievater, D. Park, and J. W. Baldwin, "Cryogenic etch process development for profile control of high aspect-ratio submicron silicon trenches," *J. Vac. Sci. Technol., B*, vol. 25, pp. 21–28, 2007.
[25] G. Barillaro, A. Nannini, and M. Piotto, "Electrochemical etching in HF solution for silicon micromachining," *Sens. Actuators, A*, vol. 102, pp. 195–201, 2002.
[26] V. A. Tolmachev, T. S. Perova, E. V. Astrova, B. Z. Volchek, and J. K. Vij, "Vertically etched silicon as 1-D photonic crystal," *Phys. Status Solidi A*, vol. 197, pp. 544–548, 2003.
[27] D. Lee, K. Yu, U. Krishnamoorthy, and O. Solgaard, "Vertical mirror fabrication combining KOH etch and DRIE of (110) silicon," *J. Microelectromech. Syst.*, vol. 18, pp. 217–227, 2009.
[28] W. H. Juan and S. W. Pang, "Controlling sidewall smoothness for micromachined Si mirrors and lenses," *J. Vac. Sci. Technol., B*, vol. 14, pp. 4080–4084, 1996.
[29] S. S. Yun, S. K. You, and J. H. Lee, "Fabrication of vertical optical plane using DRIE and KOH crystalline etching of (110) silicon wafer," *Sens. Actuators, A*, vol. 128, pp. 387–394, 2006.
[30] R. Agarwal, S. Samson, and S. Bhansali, "Fabrication of vertical mirrors using plasma etch and KOH:IPA polishing," *J. Micromech. Microeng.*, vol. 17, pp. 26–35, 2007.
[31] M. Shikida, N. Inagaki, H. Sasaki, H. Amakawa, K. Fukuzawa, and K. Sato, "The mechanism of selective corrugation removal by KOH anisotropic wet etching," *J. Micromech. Microeng.*, vol. 20, p. 015038.
[32] G. Barillaro, L. M. Strambini, V. Annovazzi-Lodi, and S. Merlo, "Optical characterization of high-order 1-D silicon photonic crystals," *IEEE J. Sel. Top. Quantum Electron.*, vol. 15, p. 1359, 2009.
[33] P. D. Atherton, N. K. Reay, J. Ring, and T. R. Hicks, "Tunable Fabry–Perot Filters," *Opt. Eng.*, vol. 20, pp. 806–814, 1981.
[34] A. V. Tikhonravov, M. K. Trubetskov, A. A. Tikhonravov, and A. Duparré, "Effects of interface roughness on the spectral properties of thin films and multilayers," *Appl. Opt.*, vol. 42, pp. 5140–5148, 2003.
[35] A. Duparré, J. Ferre-Borrull, S. Gliech, G. Notni, J. Steinert, and J. M. Bennett, "Surface characterization techniques for determining the root-mean-square roughness and power spectral densities of optical components," *Appl. Opt.*, vol. 41, pp. 154–171, 2002.
[36] R. St-Gelais, T. Kerrien, A. Poulin, and Y.-A. Peter, "In-plane MEMS tunable gires-tournois interferometers," in *Proc. Lasers Electro-Optics (CLEO) Quantum Electron. Laser Sci. Conf. (QELS)*, 2010, p. CTuW2.

Raphael St.-Gelais received the B.Eng. degree in engineering physics from Ecole Polytechnique de Montreal, Montreal, QC, Canada, in 2007. He is currently pursuing the Ph.D. degree from the same institute with the support of the Alexander Graham Bell Canada Graduate Scholarship.

He was an Engineering Intern with Dalsa Semiconductor (now Teledyne Dalsa), Bromont, QC, Canada, during a short period before joining the Microphotonics Laboratory, Ecole Polytechnique de Montreal, in 2008. His research interests include optical microelectromechanical systems, silicon photonics, and microfluidics, for applications such as biosensing, chemical sensing, and tunable components for optical fiber networks.

Alexandre Poulin received the B.Eng. degree in engineering physics from Ecole Polytechnique de Montreal (EPM), Montreal, QC, Canada in 2010. He is currently pursuing the M.Sc.A. degree from the EPM.

During his master, he made a four month long international research internship in the Center of MicroNano Technology at Ecole Polytechnique Federale de Lausanne, Lausanne, Switzerland. His current research interests include optical micro-electro-mechanical systems and optical microcavities, for applications such as integrated optical sensors and tunable semiconductor lasers.

Yves-Alain Peter (S'93–M'03–SM'07) received the M.Sc. degree in physics and the Dr.Sc. degree in sciences from the University of Neuchâtel, Switzerland, in 1994 and 2001, respectively.

In 1995, he was a Research Associate in the Medical Radiobiology Department, Paul Scherrer Institute, Switzerland. During 1995-2001, he was a Graduate Research Assistant with the Applied Optics Group, Institute of Microtechnology, University of Neuchâtel. From 2001 to 2003, he was a Postdoctoral Researcher with the Microphotonics Group, Stanford University, CA. From 2003 to 2004, he was an R&D Engineer and the Project Leader with the Swiss Center for Electronics and Microtechnology, Switzerland. He is currently an Associate Professor with the department of Engineering Physics, Ecole Polytechnique de Montréal, QC, Canada. His research interests include microphotonics and microoptoelectromechanical systems.